RSC Advances

ROYAL SOCIETY OF CHEMISTRY

www.rsc.org/advances

RSC Advances

RSC Publishing

ARTICLE

Hydrothermal synthesis of Fe_3O_4/RGO composites and investigation of electrochemical performances for energy storage application

Cite this: DOI: 10.1039/x0xx00000x

Received 00th January 2012,
Accepted 00th January 2012

DOI: 10.1039/x0xx00000x

www.rsc.org/

Sanjit Saha,[a] Milan Jana, [a,b] Pranab Samanta,[a] Naresh Chandra Murmu,[a] Nam Hoon Kim,[c] Tapas Kuila,[a] and Joong Hee Lee[c*]*

Highly porous nano-structured Fe_3O_4 particles were successfully prepared on the surface of reduced graphene oxide (RGO) sheets through one-step hydrothermal method. X-ray diffraction (XRD) and Field emission scanning electron microscopy analysis (FE-SEM) ensured not only the size and porous nature but also the formation of Fe_3O_4 and Fe_2O_3-based composites. XRD, FE-SEM and Transmission electron microscopy showed the highly crystalline nature of the particles. The reduction of graphene oxide and the formation of a few layers of RGO were confirmed by Raman spectroscopy and X-ray photoelectron spectroscopy analysis. Electrochemical performances of the Fe_3O_4/RGO composite were evaluated with two electrode configurations using nickel foam as material support as well as current collector. The synergistic effect of RGO and metal oxide were explained in terms of enhanced energy and power density, excellent electrochemical cyclic stability and low IR drop. The specific capacitance of the Fe_3O_4/RGO composite was found to be ~782 F g^{-1} at a current density of 3 A g^{-1}. The improved electrical conductivity, nanometer scale particle dimension and formation of hierarchical networks with effective redox activity contributed to the remarkable supercapacitor performance.

1. Introduction

Electrochemical capacitors (ECs) or supercapacitors store electrical energy at the electrode-electrolyte interface has attracted a significant attention as compared to a battery which stores energy through chemical reactions.[1-3] ECs can be classified as electrical double layer capacitor (EDLC) if the charges store via electrostatic way.[2] The EDLC technology is advantageous as it offers specific capacitance in the order of hundred of Farads, whereas, the result is only in the range of micro farad for the traditional dielectric capacitor.[1] In contrast, it can be termed as pseudocapacitor if the charge storage occurs through battery type redox reactions.[2] Carbon-based porous material with high specific surface area and good electrical conductivity is suitable for EC electrode material.[3] An enhanced electrochemical performance can be observed with the introduction of pseudo capacitance by incorporating metal oxide nanoparticles in the porous carbon materials.[4,5] The oxidation and reduction processes due to the participation of metal oxides enhance the charge storage capability of the supercapacitor device. However, this kind of redox reactions is not completely reversible and causes damage to the electrode materials structure resulting significant drop of specific capacitance with increasing current density.[1,4-6] The reaction between the electrolyte and electrodes affect the pseudo-capacitive nature of a particular material within the chosen potential range.[7] However, the potential window is limited within the range of 0-1.2 V in the aqueous electrolyte media.[8]

The two dimensional single layer carbon atoms, Graphene has attracted an enormous interest in supercapacitor research due to its large surface area, high mechanical strength, good chemical stability, and excellent electrical and thermal conductivity among all the carbonaceous materials reported so far.[2,9,10] However, the agglomeration of graphene results in loss of capacitive performance and other properties due to the decrease in specific surface area.[2,10] Introduction of spacer materials, like metal oxides prevent the restacking of graphene sheets during charge discharge process and further improve the capacitance performance due to the additional pseudo capacitance nature.[2,11] The use of metal oxide decorated graphene as supercapacitor electrode materials has been investigated in detail.[12] It has been found that the metal oxide/graphene hybrid nanostructures consists of very high surface area and can form a conductive network.[12-16] The presence of graphene reduces the particle size of the metal oxides in the nanometer range. It is seen that the diffusivity of the electrolyte ions decreases with increasing particle size resulting the deterioration of capacitive performances.[4] Among all these types of oxides, fabrication of Fe_3O_4 -based electrode is promising due to its low cost, low environmental impact and comparatively easy redox reaction.[12] The direct incorporation of Fe_3O_4 nanoparticles into the carbon host is suitable to form Fe_3O_4/reduced GO (RGO) hybrid composite.[12,17-19] At room temperature; the main stoichiometric forms of iron oxides are magnetite (Fe_3O_4) and hematite (Fe_2O_3) where the latter is more resistive. In hematite the iron

cations are in the Fe^{3+} state but magnetite contains both Fe^{2+} and Fe^{3+} ions.[20,21] The specific capacitances of RGO and Fe_3O_4/RGO composites are found to be 65.4 and 220.1 F g^{-1} at a current density of 0.5 A g^{-1} as reported by Wang *et al*.[12] Poisim *et al*. reported the highest specific capacitance of 86 F g^{-1} for active carbon/Fe_3O_4 composite.[4] However, the energy density values of these electrode materials were very low as compared to the commercially available batteries.

Herein, a facile hydrothermal route for the preparation of Fe_3O_4/RGO composites has been reported. Graphene oxide (GO) was used as the source of RGO and urea as reducing agent. It's a single-step process and does not require surfactant or template for the preparation of Fe_3O_4/RGO composites. The composites of Fe_3O_4/RGO were used as electrode materials for supercapacitor applications. It is anticipated that the specific capacitance and energy density values of the Fe_3O_4/RGO composite supercapacitor can fulfil the criteria of the energy storage devices. The electrochemical performances were evaluated by two electrode configuration which is more reliable as compared to the three electrode system.

2. EXPERIMENTAL STUDIES

2.1 Materials

Natural graphite flakes were purchased from Sigma-Aldrich. Hydrochloric acid, sulphuric acid, hydrogen peroxide, potassium permanganate, iron sulphate, N,N-dimethyl formamide (DMF) and sodium hydroxide were purchased from Merck, Mumbai, India. Urea was purchased from SRL, Mumbai, India. Conducting carbon black (EC-600JD, purity: >95%) and PVDF were purchased from Akzo Nobel Amides Co., Ltd, South Korea. Nickel foam was purchased from Shanghai Winfay New Material Co., Ltd., China.

2.2 Preparation of iron oxide/RGO composite

GO was prepared by modified Hummer's method following our previous publication and the final product was dried for two days inside a freeze drier (FDU-1200, Eyela, Japan).[22] Stable aqueous dispersion of GO was prepared by ultrasonication of ~ 80 mg GO in 50 ml distilled water (DI) taken a 100 ml beaker. Then, an aqueous solution of $FeSO_4.7H_2O$ (1.36 g in 20 ml of distilled water) was added to the GO dispersion followed by the addition of 5 ml 0.2M NaOH solution. The reaction mixture was then stirred for 1 h at room temperature and then transferred into a 100 ml Teflon lined stainless steel autoclave. About 3.2 g of urea was added immediately and the autoclave was sealed manually. The autoclave was then placed inside a pre-heated oven at 180 ºC for 6 h for hydrothermal reaction. Then the autoclave was allowed to cool down to room temperature and the black powder of iron oxide/RGO composites were washed, filtered thoroughly and dried under vacuum at 60 ^oC for 24 h. The obtained product was designated as FRGO1. The other two composition were prepared by varying the amount of GO and following the same procedure. The final material was termed as FRGO2 and FRGO3 for 120 and 160 mg GO, respectively. Pure Fe_3O_4 particles were prepared to compare the electrochemical performances of the composites.

2.4 Characterization

X-ray diffraction (XRD) studies of the composite were carried out at room temperature on a D/Max 2500 V/PC (Rigaku Corporation, Tokyo, Japan) at a scan rate of 1º min^{-1}(Cu Kα radiation, λ= 0.15418 nm). Field emission scanning electron microscopy (FE-SEM) images were recorded with Σigma HD, Carl Zeiss, Germany. Transmission electron microscopy (TEM) was recorded using JEOL JEM-2200 FS. For sample preparation, the composite sample was dispersed in ethanol-water mixture (~ 0.1 mg ml^{-1}) by 20 min ultra sonication followed by drop casting onto a fresh lacey carbon copper grid. Raman spectra of the samples were obtained on a Nanofinder 30 (Tokyo Instruments Co., Osaka, Japan) using Laser wavelength of 514 nm and 100 µm spot size. X-ray photoelectron spectroscopy (XPS) (Axis-Nova, Kratos Analytical Ltd., Manchester, UK) was carried out using a monochromatic Al-Kα X-ray source (1486.6 eV) from KBSI Jeonju Centre. The base pressure and dwell time were 5.2 × 10^{-9} T and 100 ms, respectively. The pass energy of the hemisphere analyzer was set at 40 and 160 eV for narrow and wide scan, respectively. The electrical conductivity was measured using four probe set up with KEITHLEY delta system consisting of AC & DC current source, model: 6221 and Nanovoltmeter model: 2182A.

Electrochemical measurements were carried out with PARSTAT 4000 (Princeton Applied Research, USA) in a two electrode symmetric configuration. The potentiostatic cyclic voltammetry (CV), galvanostatic charge discharge (CD) and electrochemical impedance spectroscopy (EIS) were carried out in 6M aqueous KOH electrolyte. The supercapacitor electrodes were prepared using the composites of 75 wt. % of Fe_3O_4/RGO hybrid, 10 wt. % PVDF and 15 wt. % carbon black dispersed into 10 ml DMF. The two pieces of nickel foam (with 1 cm diameter) were taken and about 15 drops of the above composite solution were drop casted to each of the nickel foam separately. The electrodes were dried under vacuum for 24 h at 60 ^oC. Supercapacitor assembly was used to study the performance of practical devise in two electrode system. Scheme 1 shows the schematic for the preparation of iron oxide/RGO composites and fabrication of supercapacitor device. Similar procedure was adopted for the preparation of bare Fe_3O_4 electrode to compare the results.

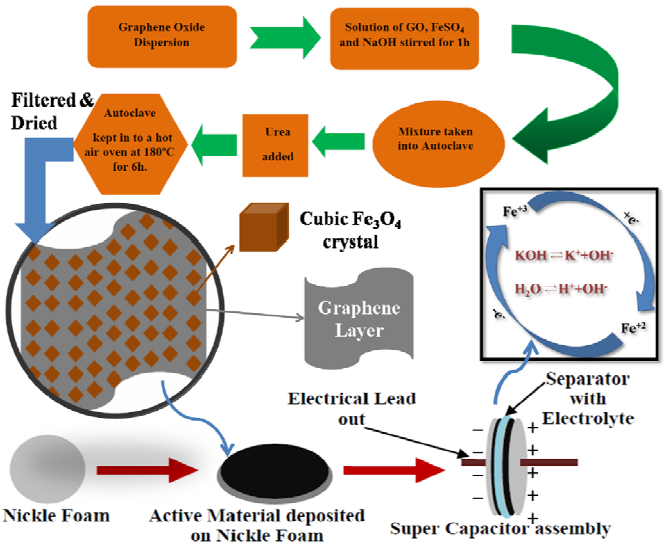

Scheme 1

3. RESULTS AND DISCUSSIONS

3.1 XRD analysis

Fig. 1 shows the XRD pattern of FRGO1, FRGO2 and FRGO3. It shows the characteristic peaks of Fe_3O_4 particles in the three composite samples.[12,23] However, the intense graphitic peak at $2\theta \approx 25\text{-}26^{o}$ was absent suggesting homogeneous exfoliation of RGO sheets in presence of Fe_3O_4 particles.[12] Some peaks of Fe_2O_3 were identified in the FRGO3 suggesting the conversion of Fe_3O_4 into Fe_2O_3 at higher content of GO.[23,24] It may be attributed to the presence of highly concentrated oxygen functional groups of GO resulting in phase transition of Fe_3O_4. The presence of sharp peaks indicated the crystalline nature of the particles coated on the graphene sheets and the peak broadening was attributed to the reduction of particle size in nanometer range.[25,26] Crystalline size of the nanoparticles was calculated according to the (311) peak line width using the Scherrer equation,

$$D = \frac{0.9\lambda}{B\cos\theta} \qquad (1)$$

Where D is the dimension of the nanoparticles, λ is the wave length of the *Kα* radiation; *B* is the 'Full Width Half Maximum' of the XRD peak, and θ is the corresponding angle.[25,26] The calculated particle sizes were 25.4, 21.9 and 25.4 nm for FRGO1, FRGO2 and FRGO3, respectively. Thus, it is seen that XRD analysis not only identifies the formation of Fe_3O_4 and Fe_2O_3 but also ensure the formation of the particles in the nanometer range.

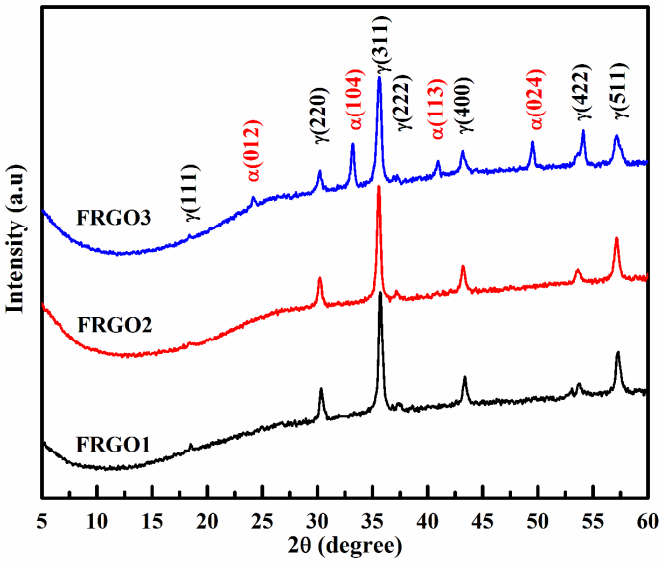

Fig. 1 XRD patterns of FRGO1, FRGO2 and FRGO3 showing peaks for γ (Fe_3O_4) and α (Fe_2O_3).

3.2 FE-SEM and TEM image analysis

FE-SEM image analysis is very useful for the investigation of surface morphology and particle size/shape. Fig. 2a shows the FE-SEM image of cubic shape Fe_3O_4 particles and the average size of the particles was recorded as 300 nm. In contrast, the size of the Fe_3O_4 particles decreased in the composites (FRGO1, FRGO2 and FRGO3) as shown in Fig. 2(b-d). All these images were recorded at lower magnification and confirmed the formation of hierarchical networks structure of the composites. In order to clearly understand the microstructure of the composites, the FE-SEM images of all the composites were recorded at higher magnification as displayed in Fig. 2(e, f). It shows homogeneous distribution of Fe_3O_4 particles in the FRGO2 composites and the presence of RGO sheets were increased in the FRGO2 and FRGO3. The inset of Fig. 2e shows the existence of nano Fe_3O_4 particles in the FRGO2 composites. In contrast, the presence of large sized tetrahedral particles of Fe_2O_3 along with the smaller cubic particles of Fe_3O_4 were present in the FRGO3 indicating the formation of two different phase iron oxide i.e. Fe_3O_4 and Fe_2O_3. This kind of distribution of phase and size agreed well with the observation of XRD analysis.

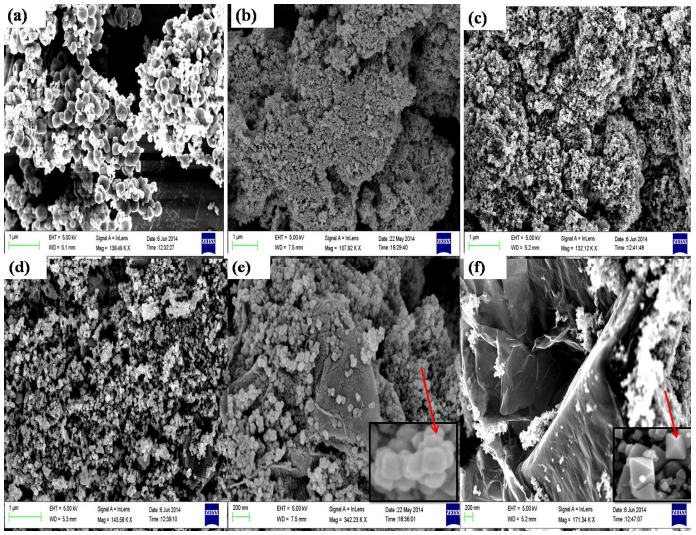

Fig. 2 Low resolution FE-SEM images of (a) Fe_3O_4, (b) FRGO1, (c) FRGO2 and (d) FRGO3. The high resolution FE-SEM image of (e) FRGO2 and (f) FRGO3 showing the graphene layers. The inset of Fig (e,f) show the formation of cubic and tetrahedral crystals of iron oxide.

TEM analysis is essential for the detailed investigation of the microstructure of the composites. Fig. 3a represents the TEM image of FRGO2, where the cubic shape particles were homogeneously distributed on the graphene sheets. The average size of the particles was in the range of ~ 20 nm. The formation of cubic shape particles and their average sizes were in good agreement with the observation of XRD and FE-SEM analysis. The highly crystalline nature of the particles was confirmed with the selected area electron diffraction (SAED) pattern image analysis (Fig. 3b).

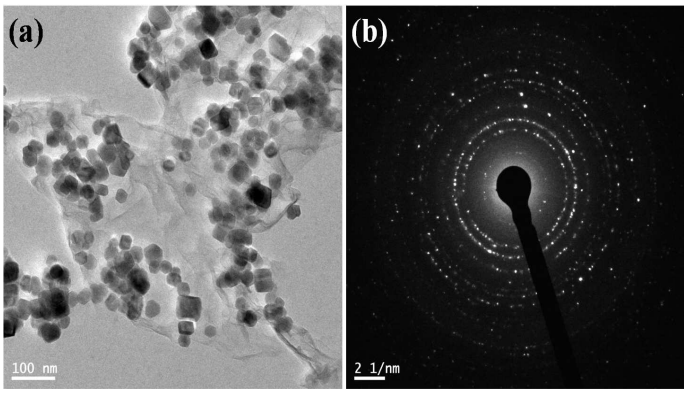

Fig. 3 (a) TEM and (b) SAED pattern images of FRGO2.

3.3 Raman spectra analysis

Electronic structure of graphite and graphene-based materials can be analysed by Raman spectroscopy which is very useful and non destructive method. Fig. 4 represents the Raman spectra of FRGO1, FRGO2 and FRGO3 composites. It showed the D and G bands at 1355 and 1575 cm^{-1}, respectively. The D band is attributed to disorder and presence of defects in the graphene lattices. In contrast, the G band is due to the highly ordered graphite and first-order scattering of the E_{2g} mode for sp^2 carbon domains.[27-29] Another peak related to the band structure of graphene layers can be observed at ~2700 cm^{-1} due to the second-order two-phonon mode and this peak distinguishes graphene from other carbon materials.[22,28] Herein, the shifting of D band towards the lower region (at 1347 cm^{-1}) was observed and the reason behind it was the defects in the graphitic plane due to the insertion of oxygen functional groups. It can be explained by the excessive oxidation of graphite and partial restoration of π-electronic conjugated network structure of RGO as supported by the XPS results.[22] The I_D/I_G ratio increased with decreasing the content of GO as starting materials and this increment indicated that the sp^3 bonds were converted to sp^2 bonds. On the other hand, the intensity of the D band decreased with increasing the GO content indicating the decrease in the amorphous nature. The I_D/I_G ratios was found to be increase with decreasing the content of GO or with increase in the percentage of iron oxide indicating the creation of extra defects and disorder on the backbone of graphene.[30] Further the broad and asymmetric 2D band confirmed the formation of few layer graphene.[22,28] The stacking and interaction between the RGO sheets and Fe_3O_4/Fe_2O_3 were the reason of this kind of broadening.[28]

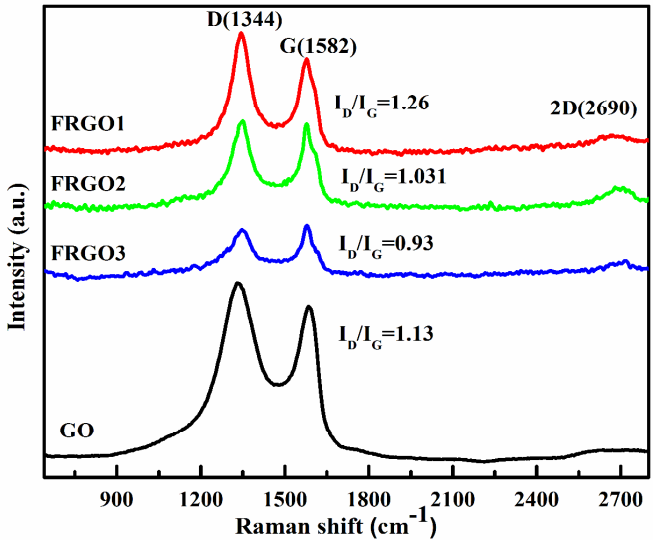

Fig. 4 Raman spectra of GO, FRGO1, FRGO2 and FRGO3.

3.4 XPS analysis

Fig. 5a represents the survey spectra of all the composite samples. The presence of C1s, O1s, Fe $2p_1$ and Fe $2p_3$ peaks can be seen for all the composites. It is seen that the intensity of the C1s and O1s peaks increased with increasing the percentage of graphene. Fig. 5b represents the high resolution Fe 2p spectra of FRGO1, FRGO2 and FRGO3. The peaks at 710.9 and 724.6 eV were attributed to the Fe $2p_{3/2}$ and Fe $2p_{1/2}$, respectively confirming the presence of Fe_3O_4 in the composite samples.[20] An additional less intense peak can be seen only in the FRGO3 at 719.9 eV, due to the presence of.[21] The presence of few amount of Fe_2O_3 along with Fe_3O_4 in the FRGO3 sample is supported by XRD and FE-SEM analysis.

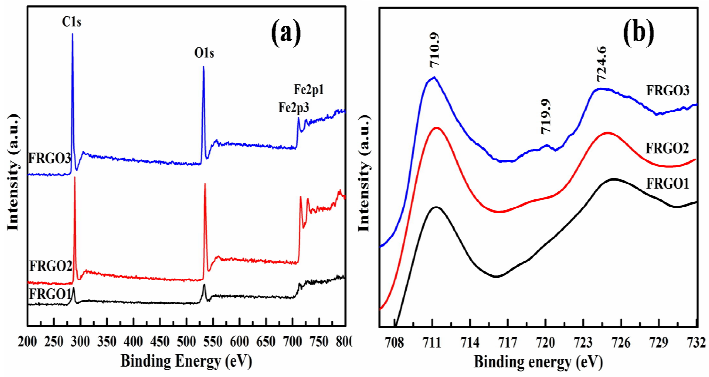

Fig. 5 (a) The survey analysis and (b) Fe2p spectra of FRGO1, FRGO2 and FRGO3.

Fig. 6a represents the high resolution C1s spectra of FRGO1. The peaks at 284.4, 285.6 and 288.6 eV correspond to the C=C, C=O and O-C=O, respectively.[2,5] Similarly, the C1s spectra of FRGO2 and FRGO3 are shown in Fig. 6(b, c). It was found that the intensities of the peaks for C=O and O-C=O functional groups were highest in the FRGO3 as

compared to that of the FRGO2 and FRGO1. It may be attributed to the decrease in level of oxidation with increasing the content of GO as starting material. The weight percentage of Fe_3O_4 in the FRGO1, FRGO2 and FRGO3 was 13.2, 10.5 and 4.7%, respectively as determined from the XPS elemental analysis.

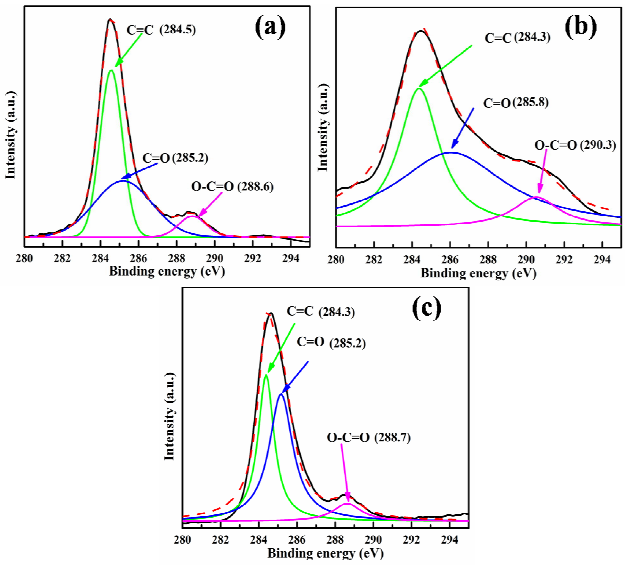

Fig. 6 C1s spectra of (a) FRGO1, (b) FRGO2 and (c) FRGO3.

3.5 Electrical conductivity

The electrical conductivity (σ) was measured by four probe methods using the formula[31]

$$\rho = \frac{\pi}{\ln 2}\frac{V}{I}d$$

$$= 4.532 \times R \times d \qquad (2)$$

$$\sigma = \frac{1}{\rho}$$

Where *V, I* and *R* are the delta voltage, current and resistance measured from the nano voltmeter. Thickness and resistivity of the samples are indicated by *d* and ρ, respectively. The high and low current ranges during the measurement were recorded in the range of 20×10^{-6} to -20×10^{-6} and the delta voltage step was fixed at 100 mV s^{-1} for all the samples. The electrical conductivity of pure Fe_3O_4 was very poor as reported earlier by Khiew *et al.*[4] A significant change in electrical conductivity (~745 times) was recorded with the introduction of graphene in the composites. The measured electrical conductivity of Fe_3O_4, FRGO1, FRGO2 and FRGO3 was recorded as 0.67, 513.6, 725.9 and 544.3 S m^{-1}, respectively. The removal of the oxygen containing groups during the reduction process made graphene sheets highly conductive and the improvement in electrical conductivity of FRGO2 was recorded. However, the electrical conductivity of the FRGO3 was significantly lower than that of the FRGO2. It may be attributed to the incomplete reduction of GO as confirmed by XPS and Raman spectroscopy. Moreover, the presence of less conducting tetrahedral Fe_2O_3 may deteriorate the electrical conductivity of the FRGO3 composites.

3.6 Electrochemical performance

CV was carried out with a potential range of 0-1.2 V with different scan rates starting from 10 to 150 mV s^{-1} (Fig. 7). The area covered by the CV curves of the composites was larger than pure Fe_3O_4 sample as shown in Fig. 7(a-d). It is seen that the response current increased with increasing the scan rates. However, the increase in current density for FRGO2 was significant among the studied samples. The better current response of FRGO2 indicated good capacitive performance. The specific capacitance of the electrode materials was measured from the CV curves using the relation,

$$C_{CV} = 4 \times \frac{\Delta q}{\Delta V \times m} \qquad (3)$$

Where the charge Δq is obtained by integrating current with the potential window for particular scan rate, ΔV is the potential window and *m* is the total active mass deposited on the electrodes.[32,33] The factor 4 is due to the two electrode system. At 10 mV s^{-1} scan rate the specific capacitance of Fe_3O_4, FRGO1, FRGO2 and FRGO3 were recorded as 74.3, 588.2, 632.3 and 550.4 F g^{-1}, respectively. The electrochemical performances of bare nickel foam and RGO were evaluated through CV and CD experiment as shown in Fig. S1-S4 (Supporting Information). The area covered by the CV curves of bare nickel foam and RGO were very low as compared to the composite electrodes. It is seen that the specific capacitance of bare nickel foam and RGO derived from CV curves were 3 and 221.6 F g^{-1} (at 10 mV s^{-1}), respectively. Fig. 8 shows the variation of specific capacitance for all the composite and pure samples with increasing scan rate. The inset view of the same figure shows the comparison of the CV plots of Fe_3O_4, FRGO1, FRGO2 and FRGO3 at a scan rate of 30 mV s^{-1}. A significant improvement in the specific capacitance in the FRGO2 composites was observed as compared to pure Fe_3O_4 sample. The increase in the peak current and the distortion of the shape of the CV curves can be observed with increasing scan rate for all the samples and is attributed to the fast redox process at high scan rate.[34] Specific capacitance of all the samples decreased with increasing scan rates. FRGO2 showed ~22.6 and 42% capacitive loss after 5 (from 10 to 50 mVs^{-1}) and 10 (from 10 to 100 mV s^{-1}) times increase in the scan rate. In contrast, these losses were 54 and 73% for pure Fe_3O_4-based electrode. At higher scan rates, the transport of electrons through the external circuits was higher than that of the diffusion of ions within the pores of the electrodes and electrolytes causing the decrease in specific capacitance. In contrast, there is an equilibrium between the adsorption and desorption of ions at the interface of the electrode/electrolyte results in the increased capacitance value.[31]

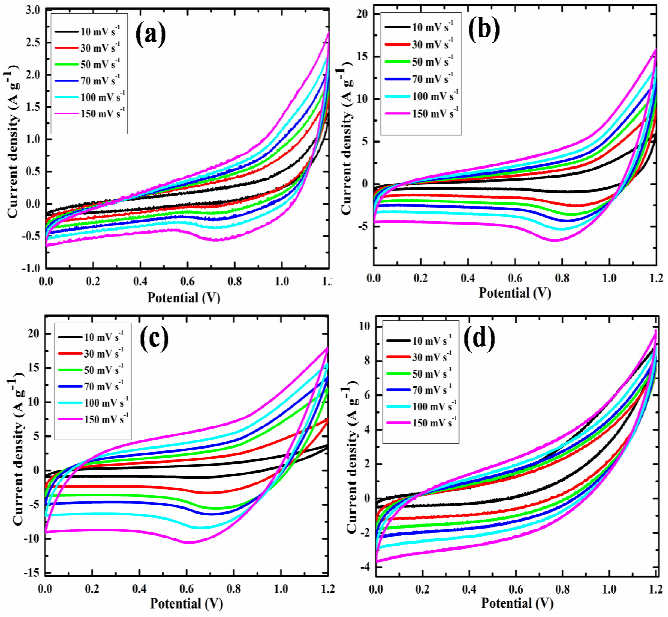

Fig. 7 CV plots of (a) Fe_3O_4, (b) FRGO1, (c) FRGO2 and (d) FRGO3.

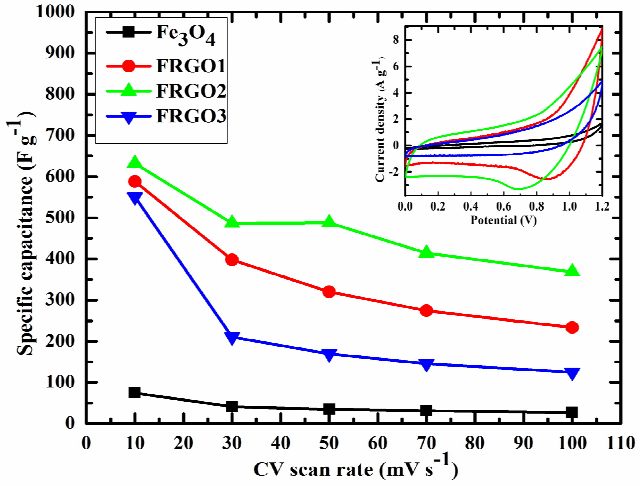

Fig. 8 Variation of specific capacitance calculated from CV with different voltage scan rate. The inset shows the comparison of the CV plots of Fe_3O_4, FRGO1, FRGO2 and FRGO3 at 30 mV s^{-1}.

The CD was also carried out within the potential range from 0-1.20 V with different charging and discharging current density (Fig. 9). The discharging time for the composite samples were much higher than that of the pure Fe_3O_4 due to the introduction of GO. In case of FRGO1, the percentage of iron was higher and results in the prominent pseudocapacitive nature during discharging and effectively increases the capacitance values. The discharging time increased further in the FRGO2 as compared to FRGO1 though pseudocapacitance as displayed in the Fig. 9 (c). However, the discharging time found to decrease in the FRGO3 suggesting the optimum content of RGO in the composites is required for supercapacitor applications. The decrease in specific capacitance may be attributed to the decrease in pseudocapacitive nature of the electrode and presence of less conducting Fe_2O_3 in the composites as evidenced from XRD and FE-SEM analysis. During sample preparation large amount of oxygen was trapped inside the autoclave reactor due to the hydrothermal reduction of GO and resulted the formation of iron oxide. It is anticipated that excess oxygen was liberated at higher content of GO in the starting materials resulting the formation of Fe_2O_3 along with the Fe_3O_4 particles. The presence of such bigger sized Fe_2O_3 particles affects the diffusive capability of electrolyte ions and also the redox reaction. Fe_3O_4 represents the normal spinal structure where the oxidation state of Fe is II and III. The inter conversion between the Fe (II) and Fe (III) provide such redox capacitance which cannot be possible for Fe_2O_3. The formation of nano-sized particles in the presence of RGO increased the specific capacitance of the composites over pure Fe_3O_4. However, for FRGO3 the formation of bigger tetrahedral particles decreased the conductivity as well as the capacitive performance. The specific capacitance of the device is best to calculated from the CD following the relation

$$C_{CD} = 4 \times \frac{\Delta t \times \mathrm{I}}{\Delta V \times m} \qquad (4)$$

Where Δt is the discharging time, I is the discharging current, ΔV is the potential range and m is the total active mass deposited on the electrodes.[32,33] The specific capacitance of Fe_3O_4, FRGO1, FRGO2 and FRGO3 are 73, 519, 782 and 553.8 F g^{-1}, respectively at a current density of 3 A g^{-1}. The specific capacitance of RGO obtained from CD curves was 238 F g^{-1} (at 3 A g^{-1}). The use of urea which can act as an expansion reducing agent during the hydrothermal process may be the reason of such highly improved performance as compared to the previously reported results.[35] The variation of specific capacitance with current density has been presented in Fig. 10 and the inset view showed the comparison of discharging profiles of all the samples at a current density of 3 A g^{-1}. It was found that the specific capacitance decreased with increasing current density and the coulombic efficiency increased for all the samples. The specific capacitance of FRGO2 was found to be 616.6 F g^{-1} at a current density of 5 A g^{-1}. The decrease in IR drop was also observed with the addition of graphene. The IR drops of the pure Fe_3O_4, FRGO1, FRGO2 and FRGO3 were recorded as 0.29, 0.08, 0.07 and 0.06 V, respectively at a current density of 3 A g^{-1}.

Fig. 11 (a) shows the coulombic efficiency of Fe_3O_4 and FRGO composite electrodes at various current densities. The coulombic efficiency of FRGO2 was recorded as ~68% at a current density of 5 A g^{-1} and the efficiency was increased to ~80% at a current density of 6.5 A g^{-1} as shown in Fig. S5 of supporting information. Table S2 (supporting information) shows that the coulombic efficiency of our system is almost comparable or even better as compared to the reported values suggesting its utility as high performance supercapacitor electrode.

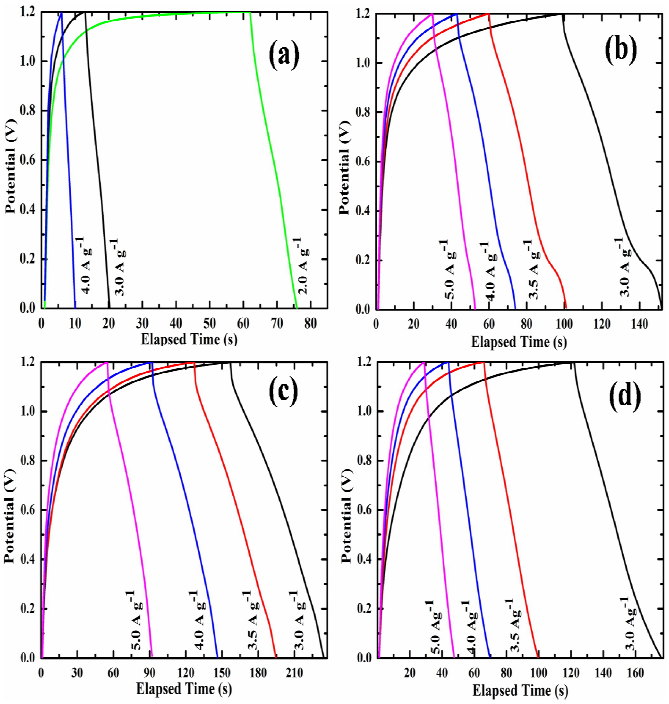

Fig. 9 CD plots of (a) Fe_3O_4, (b) FRGO1, (c) FRGO2 and (d) FRGO3.

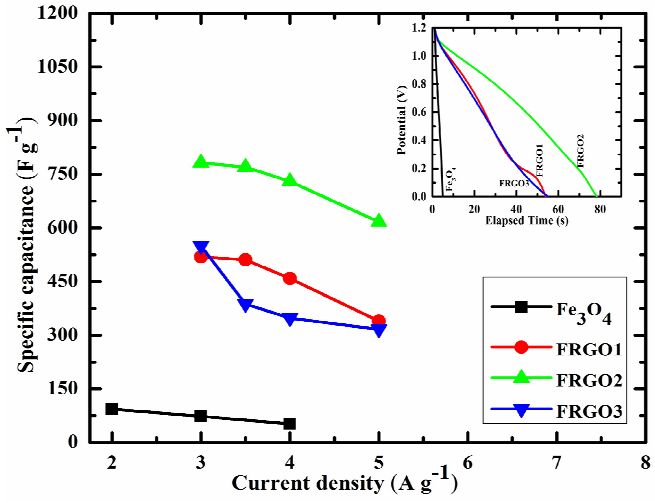

Fig. 10 Variation of specific capacitance calculated from CD with different current density. The inset shows the comparison of the CD plots of Fe_3O_4, FRGO1, FRGFO2 and FRGO3 at 3 A g^{-1}.

The energy density (E_d) and the power density (P_d) were calculated using the equations from the CD [36]

$$E_d = \frac{CV^2}{8} \qquad (5)$$

$$P_d = \frac{E_d}{\Delta t} \qquad (6)$$

Fig. 11b represents the energy density vs. power density plots of all the samples. The energy density of Fe_3O_4, FRGO1, FRGO2 and FRGO3 are 3.65, 25.95, 39.1 and 27.15 W h Kg^{-1}, respectively at a power density of 1800 W kg^{-1}. So it is seen that the energy density of the composite electrodes always remained higher as compared to the Fe_3O_4-based supercapacitor.

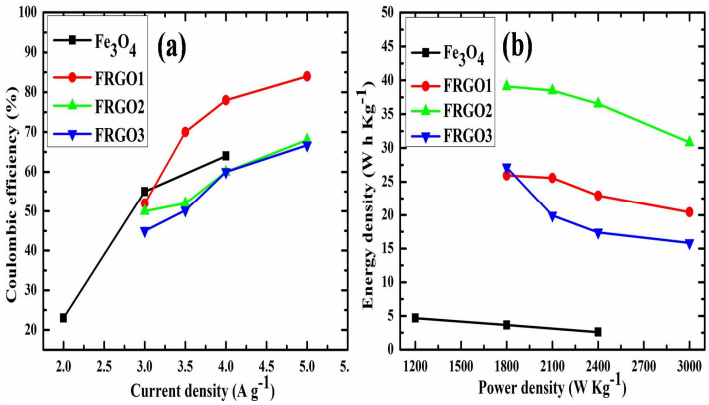

Fig. 11 (a) Coulombic efficiency vs. Current density and (b) Energy density vs. Power density plots of Fe_3O_4, FRGO1, FRGO2 and FRGO3.

The electrochemical cyclic stabilities of the pure Fe_3O_4 and the composite electrodes were measured through continuous CD process up to 1000 cycles at a constant current density of 3 A g^{-1}. Pure Fe_3O_4 showed poor cyclic stability and the value of specific capacitance decreased to 33 F g^{-1} from 73 F g^{-1} after 1000 CD cycles. On the other hand, the retention in specific capacitance for the composites was much better than that of the pure Fe_3O_4 electrode. In the case of FRGO1, the specific capacitance increased to 559 F g^{-1} from its original value of 519 F g^{-1} after 300 CD cycles and then decreased to 499 F g^{-1} after 700 cycles. The retention in specific capacitance of FRGO1 was found to be 96% after 1000 charge-discharge cycles. For FRGO2, the capacitance value first increased from 782 to 820 F g^{-1} after 300 cycles followed by decreased to 782 F g^{-1} after 600 cycles and remained stable. The retention in specific capacitance of FRGO2 was recorded as ~100% after 1000 CD. The capacitance value of FRGO3 also increased to 573 F g^{-1} (initial capacitance was 543 F g^{-1}) after 300 cycles and then decreased to 553 F g^{-1} after 500 cycles and remained stable. The initial increment in specific capacitance of the composite samples may be due to the wetting of porous electrodes by aqueous electrolyte. Fig. 12 shows that the specific capacitance of FRGO2 and FRGO3 remained almost constant after 1000 charge-discharge cycles. So it is seen that the electrochemical cyclic stability was increased with increasing the GO content in the composite samples.

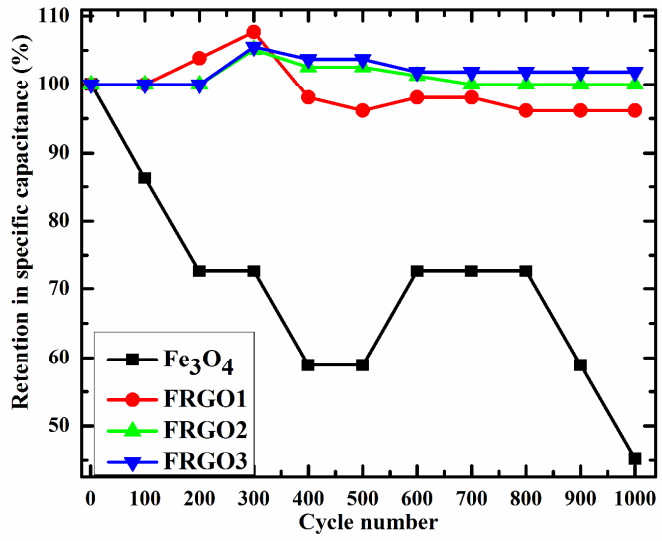

Fig. 12 Electrochemical cyclic stability profiles of Fe_3O_4, FRGO1, FRGO2 and FRGO3.

The EIS study was performed in the frequency range of 0.1 to 10^5 Hz with the amplitude of 10 mV and is represented in Fig. 13. The diffusion or the transportation of the ions between the electrolyte and the electrode surface depends on the frequency and results in a resistance element in low frequency region called Warburg resistance.[37] The lower frequency region of the pure Fe_3O_4 showed little double capacitive nature with inclination to the real or resistance axis and large Warburg resistance. Shorter Warburg indicated shorter ion diffusion path and steeper Warburg suggested good formation rate of electric double layer.[2] Fig. 13 clearly shows the improvements in diffusion path and formation of double layer as well as enhanced capacitive performance with the addition of GO. Faradaic resistance and the height of the pseudo-semicircle region decreased with increasing GO content in the composites indicating good electrochemical performance or high capacitive nature. The inclination of the straight line at lower frequency region towards the imaginary axis indicated porous and conductive nature of the electrode materials. It was found that the slope of the straight line was higher for the FRGO2 composites as compared to other samples. The frequency dependent ion diffusion or the charge transportation in the high frequency region also generated a resistance called the solution resistance and can be measured directly from the intersection at the real axis. The solution resistance values were 2.52, 0.418, 0.256 and 1.468 Ω for Fe_3O_4, FRGO1, FRGO2 and FRGO3, respectively as determined from the EIS spectra (inset of Fig. 13). These observations are well supported by the CV and CD analysis indicating the best electrochemical performance of FRGO2. The lower solution resistance provided good path between the electrodes and the maximum power density (P_{max}) of the device also can be calculated following the relation

$$P_{\max} = \frac{V_i^2}{4MR} \qquad (7)$$

Where V_i is the initial voltage or the voltage window, R is the solution resistance and M is the total deposited mass.[37] Following the relation it is observed a huge improve in the power density from 600.2 W Kg^{-1} to 2812.5 W Kg^{-1} for the FRGO2 over pure (Fe_3O_4) one. The electrochemical performances of the Fe_3O_4/RGO composites have been compared in Table S2 of supporting information. It is seen that the Fe_3O_4/RGO composites can be used as supercapacitor electrode materials for energy storage applications due to its comparable electrochemical performances.

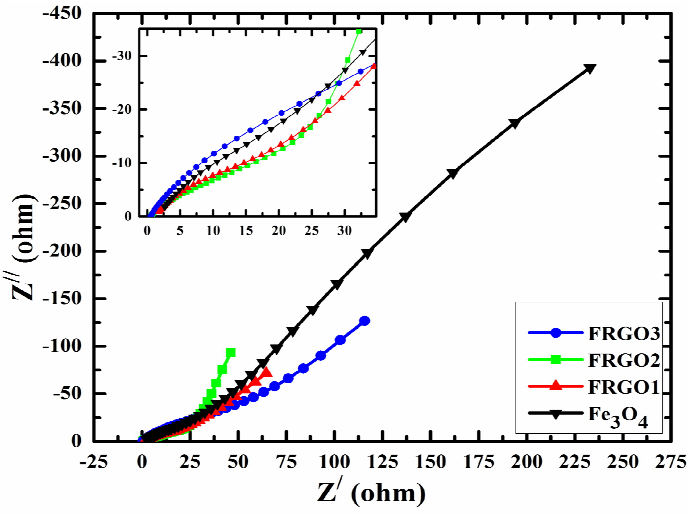

Fig. 13 Nyquist plots of Fe_3O_4, FRGO1, FRGO2 and FRGO3. The inset shows the high frequency intercept region.

4. Conclusions

The Fe_3O_4/rGO composites were successfully prepared through hydrothermal reaction and the effect of formation of porous graphene conductive network on supercapacitor application was well established. The sample FRGO2 was found to be best among the studied samples with a specific capacitance of 782 F g^{-1} at current density 3 A g^{-1}. The energy density and power density were found to be 39.1 W h Kg^{-1} and 1800 W Kg^{-1}, respectively. The formation of conductive network and Fe_3O_4 particles might have improved the capacitive performance of the FRGO2 and compared to the FRGO1. Both the electrical conductivity and capacitive performances were decreased in the FRGO3 due to the presence of bigger non conducting tetrahedral particles of Fe_2O_3 and partial removal of oxygen containing functional groups. Further the absence of pseudocapacitive nature due to the lower amount of metal oxide may be the reason of comparable poor performance of FRGO3. All these electrochemical studies were supported by the XRD, FE-SEM, RAMN and XPS analysis. Thus, it is seen that the formation of hybrid nanostructure with proper stoichiometric ratios of the reactants can produce highly efficient electrode materials for supercapacitor device for energy storage applications.

Acknowledgments

This study was supported by the INSPIRE Faculty Scheme, DST, New Delhi, India and CSIR New Delhi, India. Authors are also thankful to Dr. P. Pal Roy, the Director of CSIR-CMERI, Durgapur, India.

Notes and references

[a] *Surface Engineering & Tribology Division, CSIR-Central Mechanical Engineering Research Institute, Durgapur -713209, India*
[b] *Academy of Scientific and Innovative Research (AcSIR), Anusandhan Bhawan, 2 Rafi Marg, New Delhi-110001, India*
[c] *Applied Materials Institute for BIN Convergence (BK Plus Global Program), Department of BIN Fusion Technology, Chonbuk National University, Jeonju, Jeonbuk, 561-756, Republic of Korea.*
[*] *Correspondence to Tapas Kuila (91-9647205077; Fax: 91-343-2548204; E-mail: tkuila@gmail.com) and Joong Hee Lee (jhl@jbnu.ac.kr)*

1. H. Ji, X. Zhao, Z. Qiao, J. Jung, Y. Zhu, Y. Lu, L. L. Zhang, A. H. MacDonald and R.S. Ruoff, *Nat. Commun.* DOI: 10.1038/ncomms4317.
2. Y. Lu, F. Zhang, T. Zhang, K. Leng, L. Zhang, X. Yang, Y. Ma, Y. Huang, M. Zhang and Y. Chen, *Carbon*, 2013, **63**, 508-516.
3. E. Paek, A. J. Pak, K. E. Kweon, and G. S. Hwang, *J. Phys. Chem*, 2012
4. P. Khiew, M. Ho, T.Tan, W. Chiu, R. Shamsudin, M. A. Hamid, and C. H. Chia, *Int. J. Chem: Mater. Sci. Eng.*, 2013, **7**,8.
5. C. Xiang, M. Li, M. Zhi, A. Manivannan, N. Wu, *J. Power Sources*, 2013, **226**, 65-70.
6. S. L. Zhang, Y. M. Li, N. Pan. *J. Power sources*, 2012, **206**, 476-482.
7. D. Qu, *J appl Electrochem*, 2009, **39**, 867-871.
8. Electrochemical Supercapacitors (Scientific Fundamentals and Technological Applications), B.E Conway, (page 28,265).
9. A. Yu, A. Sy, A. Davies, *Synth. Met*., 2011,**161**, 2049– 2054.
10. Z. Fan, Q. Zhao, T. Li, J. Yan, Y. Ren, J. Feng and T. Wei, *Carbon*, 2012, **50**, 1699-1712.
11. C. Liang, T. Zhai, W. Wang, J. Chen, W. Zhao, X. Lu and Y. Tong, *J. Mater. Chem. A*, 2014, **2**, 7214.
12. Q. Wang, L. Jiao, H. Du, Y. Wang and H.Yuan, *J. Power Sources*, 2014, **245**, 101-106.
13. Z.-S. Wu, D.-W. Wang, W. Ren, J. Zhao, G. Zhou, F. Li and H.-M. Cheng, *Adv. Funct. Mater*., 2010, **20**, 3595-3602.
14. Z. Fan, J. Yan, T. Wei, L. Zhi, G. Ning, T. Li and F. Wei, *Adv. Funct. Mater*., 2011, **21**, 2366-2375.
15. S. Chen, J. Zhu, X. Wu, Q. Han and X. Wang, *ACS Nano.*, 2010, **4**, 2822-2830.
16. X. Lu, Y. Zeng, M. Yu, T. Zhai, C. Liang, S. Xie, M. S. Balogun and Yexiang Tong, *Adv. Mater*. 2014, **26**, 3148-3155.
17. W. Shi, J. Zhu, D.H. Sim, Y.Y. Tay, Z. Lu, X. Zhang, Y. Sharma, M. Srinivasan, H. Zhang, H.H. Hng and Q. Yan, *J. Mater. Chem.*, 2011, **21**, 3422-3427.
18. J. Mu, B. Chen, Z. Guo, M. Zhang, Z. Zhang, P. Zhang, C. Shao and Y. Liu, *Nanoscale*, 2011, **3**, 5034-5040.
19. Y. He, L. Huang, J.-S. Cai, X.-M. Zheng and S.-G. Sun, *Electrochim. Acta*, 2010, **55**, 1140-1144.
20. W. Yan1, M. A. V. Ramos, B. E. Koel and W. Zhang, *Chem. Commun.,* 2010,
21. M. Aronniemi, J. Lahtinen and P. Hautojärvi, *Surf. Interface Anal.,* 2004, **36**, 1004-1006.
22. M. Jana, S. Saha, P. Khanra, N. C. Murmu, S. K. Srivastava, T. Kuila and J. H. Lee, *Mater. Sci. Eng.,B*, 2014, **186**, 33-40.
23. Y. Penga, C. Park and D. E. Laughlin, *J. Appl. Phys*., 2013, **93**, 10.
24. M.N. Batin and V. Popescu, *Powder Metallurgy Progress*, 2011, **11**, 3-4.
25. J. Sun, S. Zhou, P. Hou, Y. Yang, J. Weng, X. Li and M. Li, *J Biomed Mater Res A*, DOI 10.1002/jbm.a.
26. O. Rahman, S. C. Mohapatra and S. Ahmad, *Mater. Chem. Phys*., 2012, **132**, 196-202.
27. K. N. Kudin, B. Ozbas, H.C. Schniepp, R. K. Prud'homme, I. A. Aksay and R. Car, *Nanao Letters*, 2008, **8**, 36-41.
28. D. Deng, X. Pan, H. Zhang, Q. Fu, D. Tan and X. Bao, *Adv. Mater.*, 2010, **22**, 1-4.
29. A. C. Ferrari, J. C. Meyer, V. Scardaci, C. Casiraghi, M. Lazzeri, F. Mauri, S. Piscanec, D. Jiang, K. S. Novoselov, S. Roth and A. K. Geim, *Phys. Rev. Lett*., 2006, **97**, 187401.
30. F. P. Du, J. J. Wang, C. Y. Tang, C. P. Tsui, X. L. Xiec and K. F. Yung, *Composites: Part B*, 2013, **53**, 376–381.
31. S. Dhibar, P. Bhattacharya, G. Hatui, S. Sahoo and C. K. Das, *ACS Sustainable Chem. Eng*., 2013,
32. M. D. Stoller and R. S. Ruoff, *Energy Environ. Sci.,* 2010, **3**, 1294-1301.
33. P. Ramya and M. V. Sangaranaryanan, *J. Chem. Sci.,* 2008, **120**, 25-31.
34. J. M. Luo, B. Gao and X. G. Zhang, *Mater. Res. Bull*., 2008, **43**, 1119-1125.
35. S. Wakeland, R. Martinez, J. K. Grey, C. C. Luhrs, *Carbon*, 2010, **48**, 3463-3470.
36. Y. Chang, G. Han, J. Yuan, D. Fu, F. Liu and S. Li, *J. Power Sources*, 2013, **238**, 492-500.
37. R.B. Rakhi and H.N. Alshareef, *J. Power Sources*, 2011,**196**, 8858-8865.

Graphical Abstract